Science Advances
AAAS

advances.sciencemag.org/cgi/content/full/6/42/eabb5953/DC1

# Supplementary Materials for

## Transcriptional suppression of ribosomal DNA with phase separation

Satoru Ide*, Ryosuke Imai, Hiroko Ochi, Kazuhiro Maeshima*

*Corresponding author. Email: kmaeshim@nig.ac.jp (K.M.); satide@nig.ac.jp (S.I.)

Published 14 October 2020, *Sci. Adv.* **6**, eabb5953 (2020)
DOI: 10.1126/sciadv.abb5953

**The PDF file includes:**



**Other Supplementary Material for this manuscript includes the following:**

(available at advances.sciencemag.org/cgi/content/full/6/42/eabb5953/DC1)

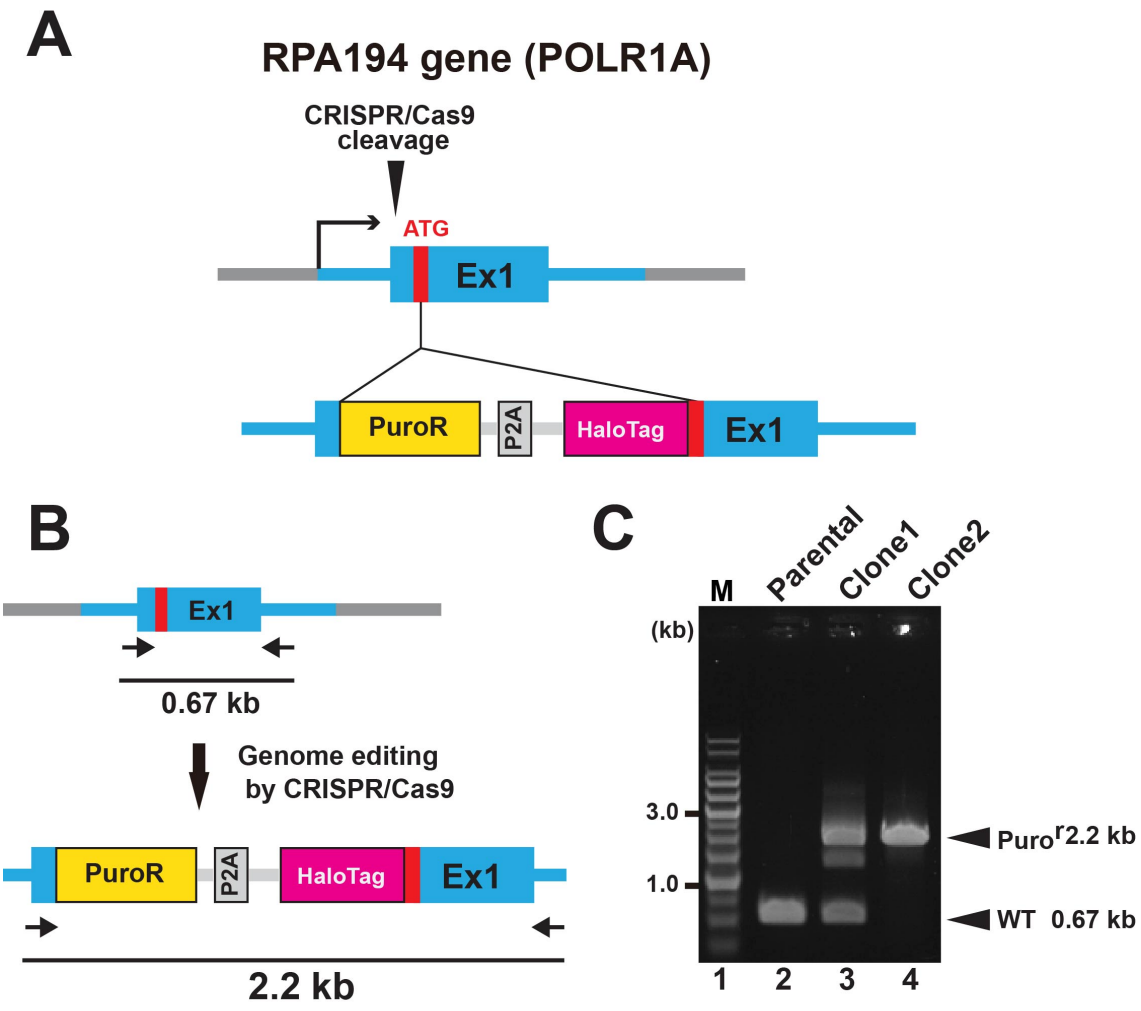
A
RPA194 gene (POLR1A)
CRISPR/Cas9
cleavage
ATG
Ex1
PuroR
P2A
HaloTag
Ex1
B
Ex1
0.67 kb
Genome editing
by CRISPR/Cas9
PuroR
P2A
HaloTag
Ex1
2.2 kb
C
M
Parental
Clone1
Clone2
(kb)
3.0
1.0
Puro^r 2.2 kb
WT 0.67 kb
1
2
3
4

fig. S1

**Figure S1. Knock-in of HaloTag-RPA194 through genome editing. (A)** Diagram of CRISPR/Cas9-mediated homologous recombination for inserting an antibiotic resistance gene and HaloTag at the N-terminus of the RPA194 gene. The genomic sequence used in the donor plasmid homologous arms is shown in blue. PuroR, puromycin resistant gene; P2A, ribosomal skipping signal. (**B**) Genotyping using polymerase chain reaction (PCR) to detect tagging of RPA194 with HaloTag. Expected PCR products and the primers used are shown. After HaloTag integration at the N-terminus of the RPA194 locus, PCR was expected to produce a 2.2-kb product from Clones 1 and 2, and a 0.67-kb product from the parental cells and Clone 1. **(C)** Result of agarose gel electrophoresis of the PCR products from genomic DNA. M, 1-kb ladder marker.

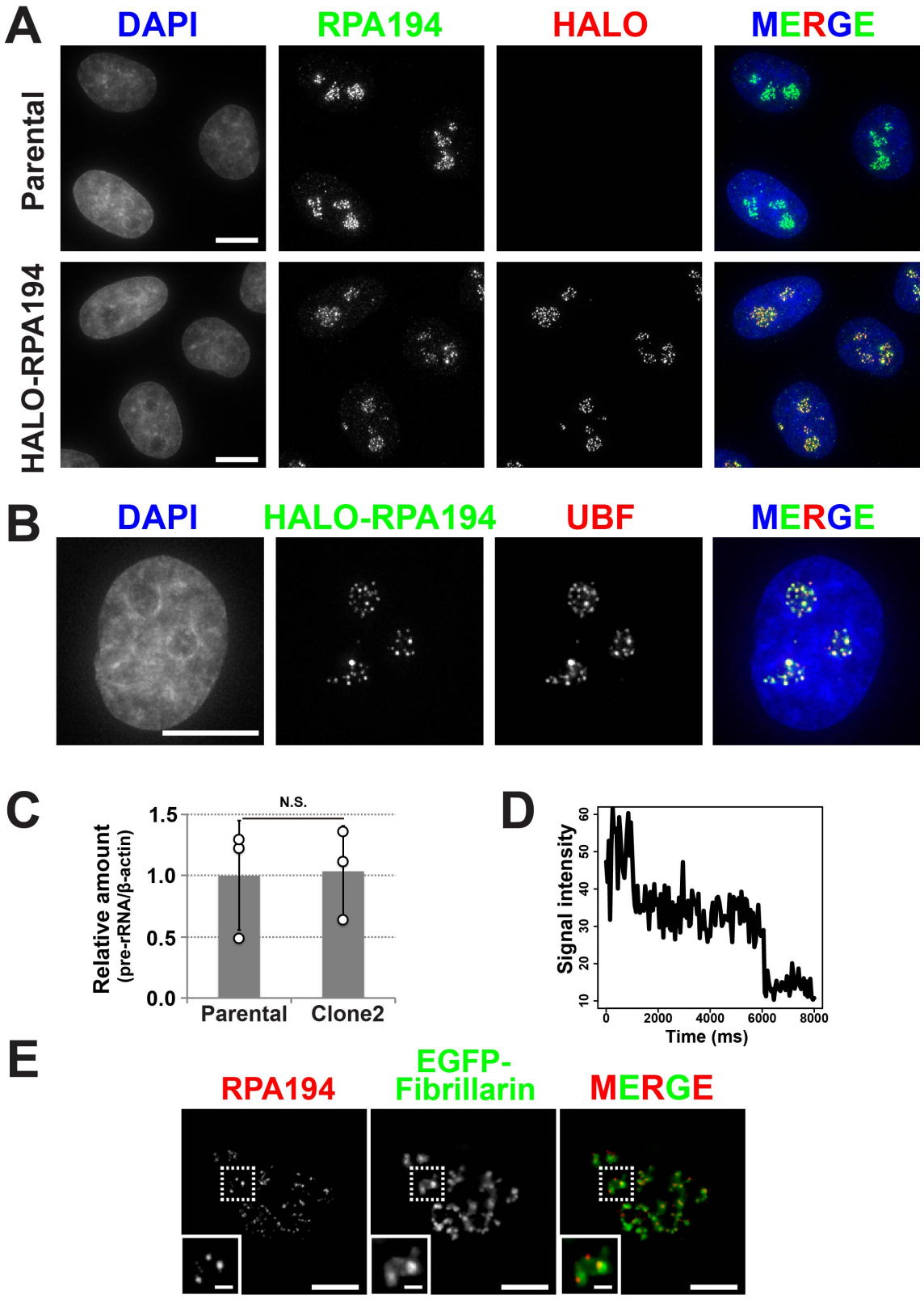
A
DAPI
RPA194
HALO
MERGE
Parental
HALO-RPA194
B
DAPI
HALO-RPA194
UBF
MERGE
C
N.S.
Relative amount
(pre-rRNA/β-actin)
1.5
1.0
0.5
0.0
Parental
Clone2
D
Signal intensity
60
50
40
30
20
10
0
2000
4000
6000
8000
Time (ms)
E
RPA194
EGFP-
Fibrillarin
MERGE

fig. S2

**Figure S2. HaloTag-labeled RPA194 foci in the Clone 2 cell.**

**(A)** Immunostaining of RPA194 and simultaneous fluorescent labeling of RPA194 with an excess amount of the TMR-HaloTag ligand. Scale bar, 10 μm. **(B)** Immunostaining of upstream binding factor (UBF) and simultaneous fluorescent labeling of RPA194 with an excess amount of the TMR-HaloTag ligand. Scale bar, 10 μm. **(C)** Pre-rRNA synthesis levels in parental HeLa cells and Clone 2. We assayed 47S pre-rRNA levels using quantitative PCR (qPCR) and normalized the data to β-actin mRNA levels. Error bars represent standard deviation calculated from three independent experiments. NS, no significance; $P > 0.9$, two-tailed unpaired Student's *t*-test. **(D)** An exceptional example of two-step photobleaching of the HaloTag-RPA194 dot. **(E)** Simultaneous visualization of HaloTag-RPA194 (red) and EGFP-fibrillarin (green) in a live cell. Note that HaloTag-RPA194 was fluorescently labeled with an excess amount of the HaloTag ligand TMR. Scale bars, 5 μm. Insets show enlarged images of the boxed region. Scale bars, 2 μm.

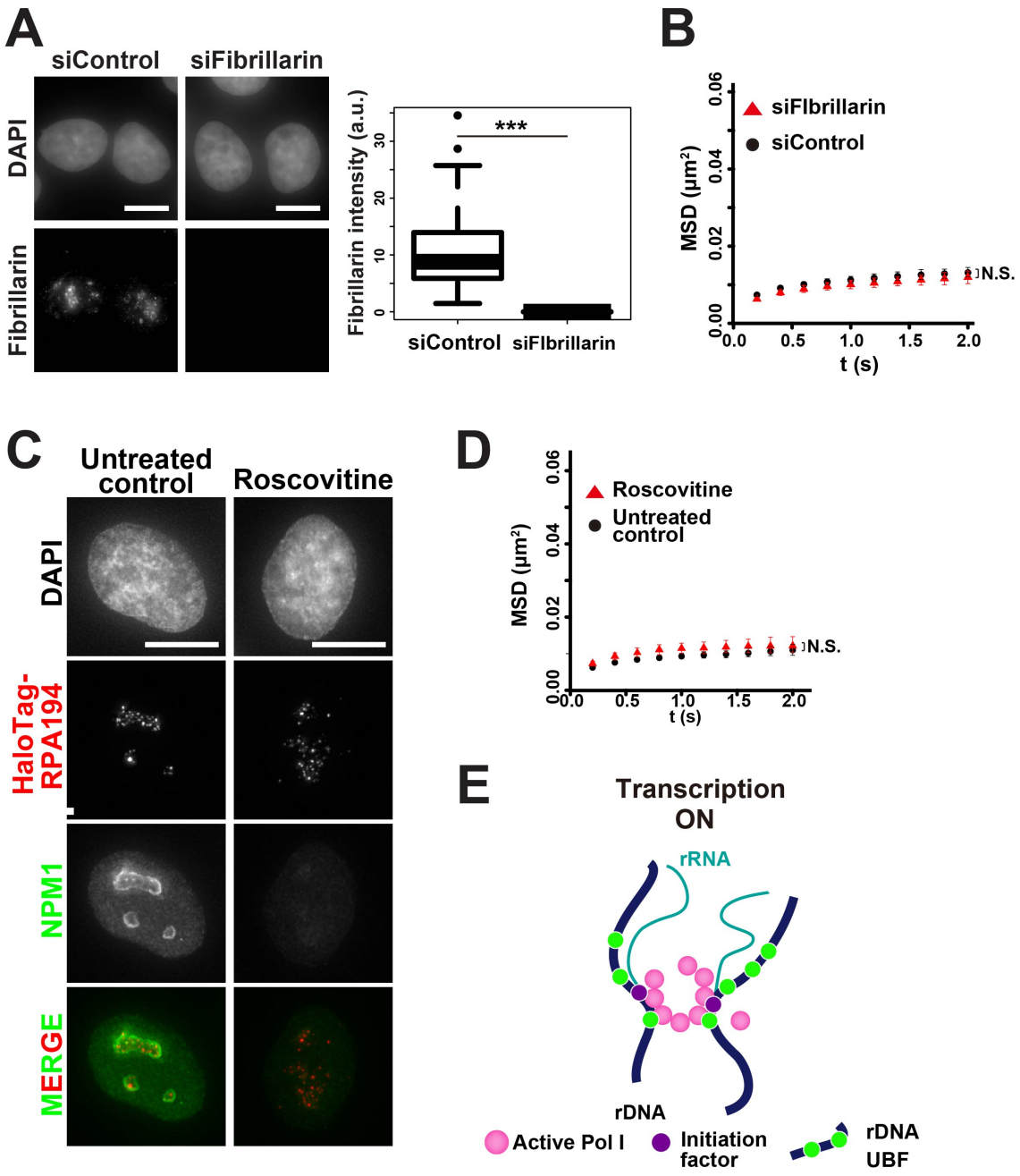
A
siControl
siFibrillarin
DAPI
Fibrillarin
Fibrillarin intensity (a.u.)
***
siControl
siFIbrillarin
B
siFIbrillarin
siControl
MSD (µm²)
N.S.
t (s)
C
Untreated control
Roscovitine
DAPI
HaloTag-RPA194
NPM1
MERGE
D
Roscovitine
Untreated control
MSD (µm²)
N.S.
t (s)
E
Transcription ON
rRNA
rDNA
Active Pol I
Initiation factor
rDNA UBF

fig. S3

**Figure S3. Dynamics of Pol I following inhibition of post-transcriptional rRNA maturation. (Left, A)** knockdown (KD) of fibrillarin by small interfering RNA (siRNA). Cells were transfected with siRNA for non-target control (siControl) or fibrillarin (siFibrillarin) and incubated for 60 h. KD efficiency was confirmed via fibrillarin immunostaining. **(Right, A)** quantification of the signal intensity of fibrillarin foci in siControl- (siControl, n = 86) and siFibrillarin-transfected cells (siFibrillarin, n = 85). Scale bars, 10 μm. Median values were compared using the Wilcoxon rank sum test (***$P < 0.001$). **(B)** MSD plots of HaloTag-RPA194 in siControl- (black) and siFibrillarin- (red) transfected cells. **(C)** Localization of TMR-Halo-RPA194 labeled with excess amounts of TMR and nucleophosmin (NPM1) in roscovitine-treated cells. NPM1 was detected using an antibody. No prominent effects of Halo-RPA194 localization were observed in roscovitine-treated cells. Scale bar, 10 μm. (**D**) MSD plots of HaloTag-RPA194 in roscovitine-treated (red) and control (black) cells. **(E)** Active Pol I molecules form a stable cluster/condensate for transcription of rRNA genes (rDNA), thus constraining rDNA chromatin.

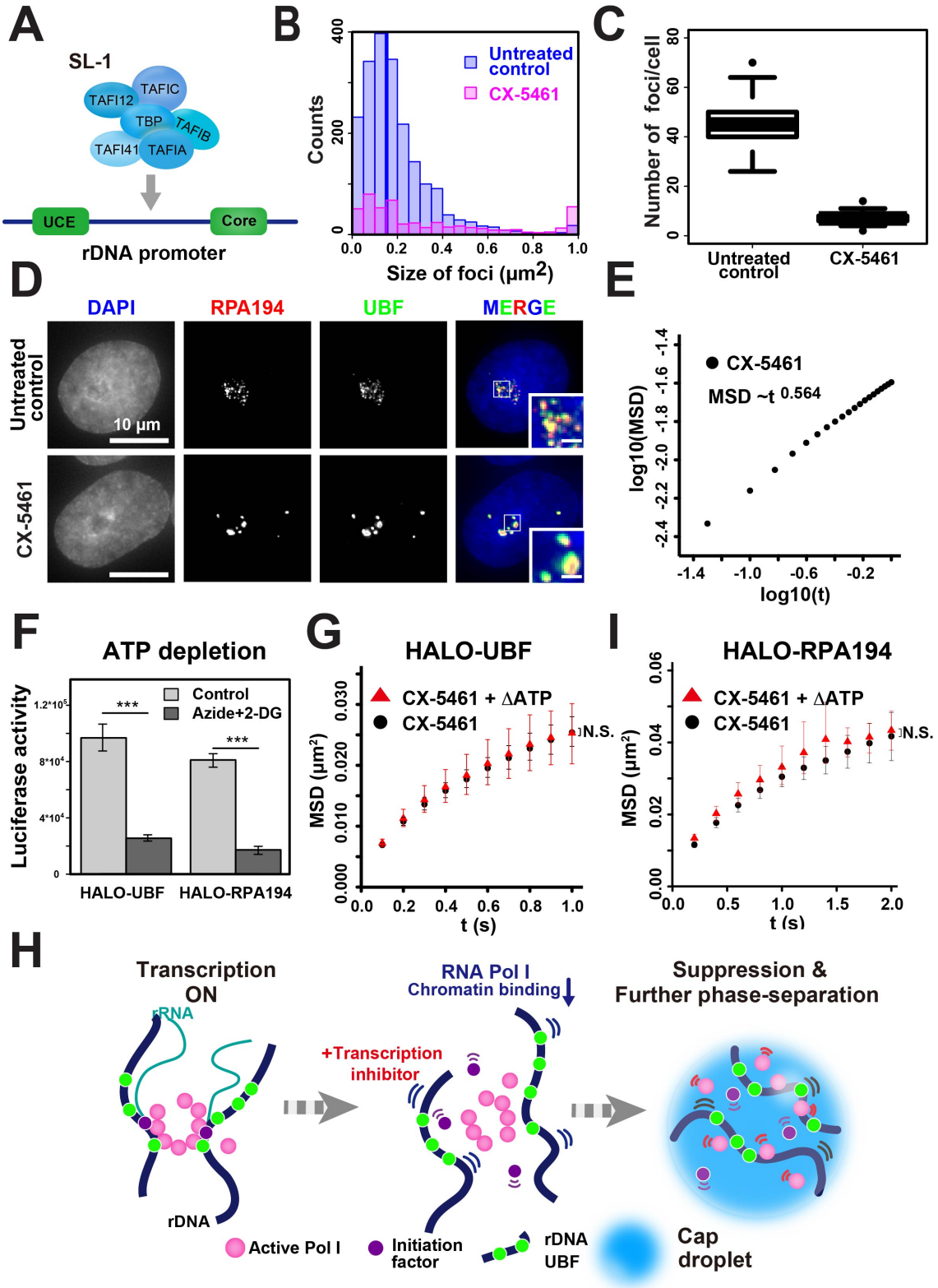
A
SL-1
TAFIC
TAFI12
TBP
TAFIB
TAFI41
TAFIA
UCE
Core
rDNA promoter
B
Untreated control
CX-5461
Counts
Size of foci (μm2)
C
Number of foci/cell
Untreated control
CX-5461
D
DAPI
RPA194
UBF
MERGE
Untreated control
CX-5461
10 μm
E
CX-5461
MSD ~t 0.564
log10(MSD)
log10(t)
F
ATP depletion
Luciferase activity
Control
Azide+2-DG
***
HALO-UBF
HALO-RPA194
G
HALO-UBF
CX-5461 + ΔATP
CX-5461
N.S.
MSD (μm2)
t (s)
I
HALO-RPA194
CX-5461 + ΔATP
CX-5461
N.S.
MSD (μm2)
t (s)
H
Transcription ON
rRNA
rDNA
+Transcription inhibitor
RNA Pol I Chromatin binding
Suppression & Further phase-separation
Active Pol I
Initiation factor
rDNA UBF
Cap droplet

fig. S4

**Figure S4. Dynamics of Pol I following transcription inhibitor treatment.**
**(A)** Diagram of the SL-1 complex binding to the rDNA promoter. **(B)** Focus size distribution of TMR-HaloTag-RPA194 in Clone 2 cells with and without CX-5461 treatment. **(C)** The number of TMR-HaloTag-RPA194 foci in Clone 2 cells with and without CX-5461 treatment. **(D)** Localization of fluorescently labeled HaloTag-RPA194 and UBF in an untreated control HeLa cell (first row) and a cell treated with CX-5461 (second row) determined via immunostaining. First column, DAPI staining; second column, TMR-HaloTag-RPA194; third column, UBF; fourth column, merged images. Scale bars, 10 μm. Insets show enlarged images of regions indicated with boxes. Scale bars, 1 μm. **(E)** Log–log plot of UBF MSD with transcription inhibitor treatment (see Figure 2D). **(F)** Verification of ATP depletion based on luciferase activity, showing successful reduction of intracellular ATP levels in HeLa cells expressing HaloTag-RPA194 (right) and HaloTag-UBF (left) treated with sodium azide and 2-deoxy-glucose. ***$P < 0.001$, two-sided unpaired Student's *t*-test (error bars ± SD) for the control versus drug-treated cells expressing HALO-RPA194 ($P = 2.3 \times 10^{-4}$) and HALO-UBF ($P = 3.8 \times 10^{-5}$). **(G)** MSD plots of HaloTag-UBF chromatin in ATP-depleted cells following CX-5461 treatment with 95% CIs. CX-5461-treated cells were incubated with (red, n = 21 cells) or without (black, n = 19 cells) 50 mM 2-deoxyglucose and 10 mM sodium azide for 30 min. N.S., not significant; P = 0.96. **(Center, H)** After transcription inhibition, the Pol I cluster/condensate detaches from chromatin, thereby releasing the chromatin constraint. **(Right)** Pol I behaves like a liquid in the nucleolar cap through phase separation. **(I)** MSD plots of HaloTag-RPA194 molecules in ATP-depleted cells following CX-5461 treatment. CX-5461-treated cells were incubated with (red, n = 21 cells) or without (black, n = 19 cells) 50 mM 2-deoxyglucose and 10 mM sodium azide for 30 min. Data are plotted with 95% CIs. N.S., not significant; P = 0.35.

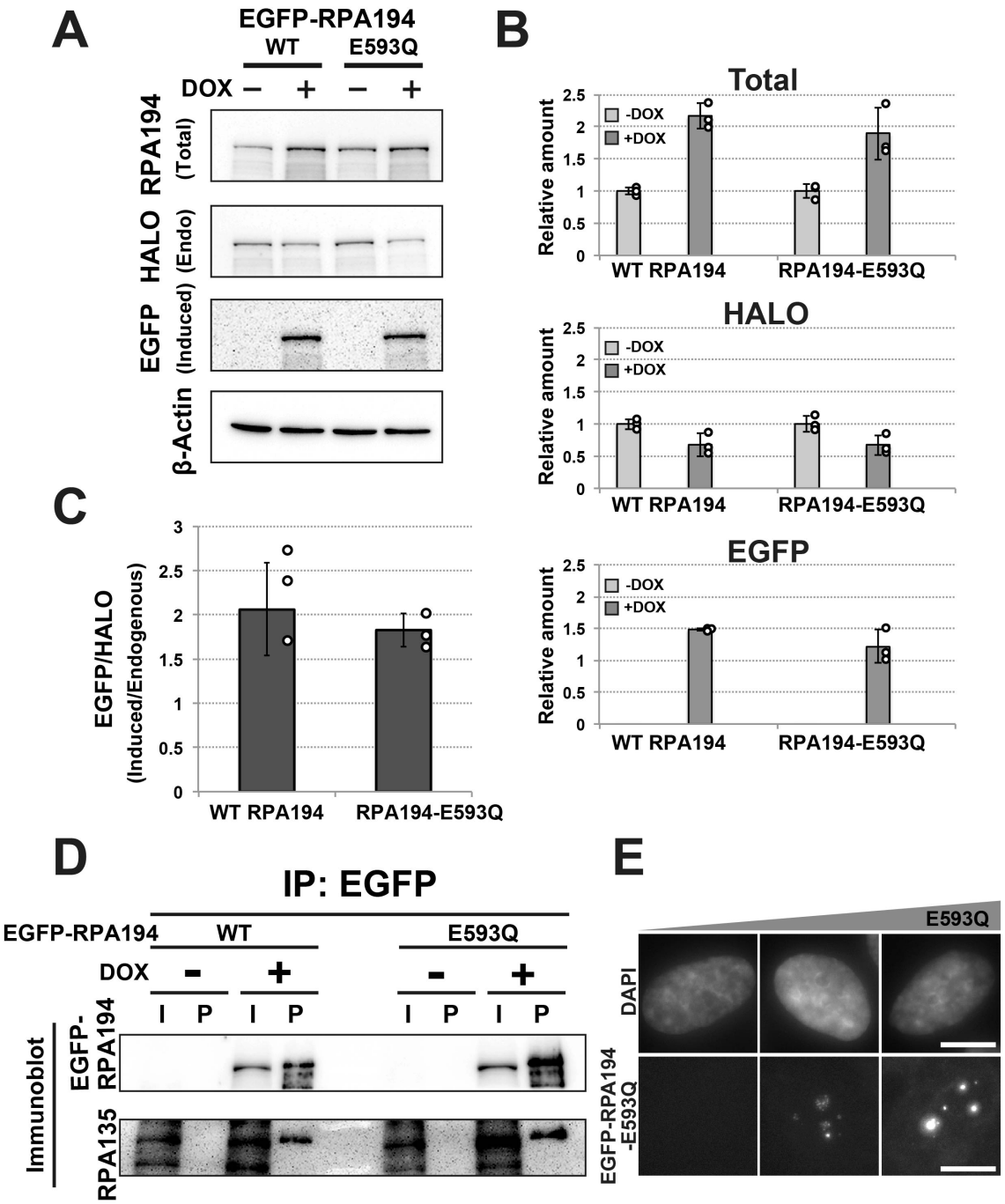
A
EGFP-RPA194
WT
E593Q
DOX – + – +
RPA194 (Total)
HALO (Endo)
EGFP (Induced)
β-Actin
B
Total
HALO
EGFP
Relative amount
-DOX
+DOX
WT RPA194
RPA194-E593Q
C
EGFP/HALO
(Induced/Endogenous)
D
IP: EGFP
EGFP-RPA194
WT
E593Q
DOX - + - +
I P I P I P I P
Immunoblot
EGFP-RPA194
RPA135
E
E593Q
DAPI
EGFP-RPA194-E593Q

fig. S5

**Figure S5. Expression of RPA194-E593Q and comparison with endogenous RPA194.**

**(A)** Immunoblotting to quantify amounts of endogenous HaloTag-RPA194 and induced EGFP-RPA194. Total RPA194, HaloTag-RPA194, EGFP-RPA194, and β-actin were detected using anti-RPA194, anti-HaloTag, anti-GFP, and anti-β-actin antibodies, respectively. **(B)** Quantification of protein levels of total RPA194, endogenous HaloTag-RPA194, and induced EGFP-RPA194 and RPA194 E593Q. The intensity of each blot signal in (A) was normalized to that of β-actin. (**C**) The ratio of induced EGFP-RPA194 (and EGFP-RPA194-E593Q) to endogenous HaloTag-RPA194 was calculated from (B). The induced EGFP-RPA194 level was approximately two-fold greater than that of endogenous HaloTag-RPA194. (**D**) Co-immunoprecipitation of the two largest subunits in the mutant Pol I complex, RPA135 and EGFP-RPA194-E593Q. Extracts of cells expressing EGFP-RPA194 (WT) and EGFP-RPA194-E593Q (E593Q) were immunoprecipitated using the anti-green fluorescent protein (GFP) antibody. We subjected 5% of the input fraction (I) and pulldown fraction (P) to immunoblotting of EGFP-RPA194 and RPA135. (**E**) Distribution change of EGFP-RPA194-E593Q upon increase of its expression. Scale bars, 10 μm.

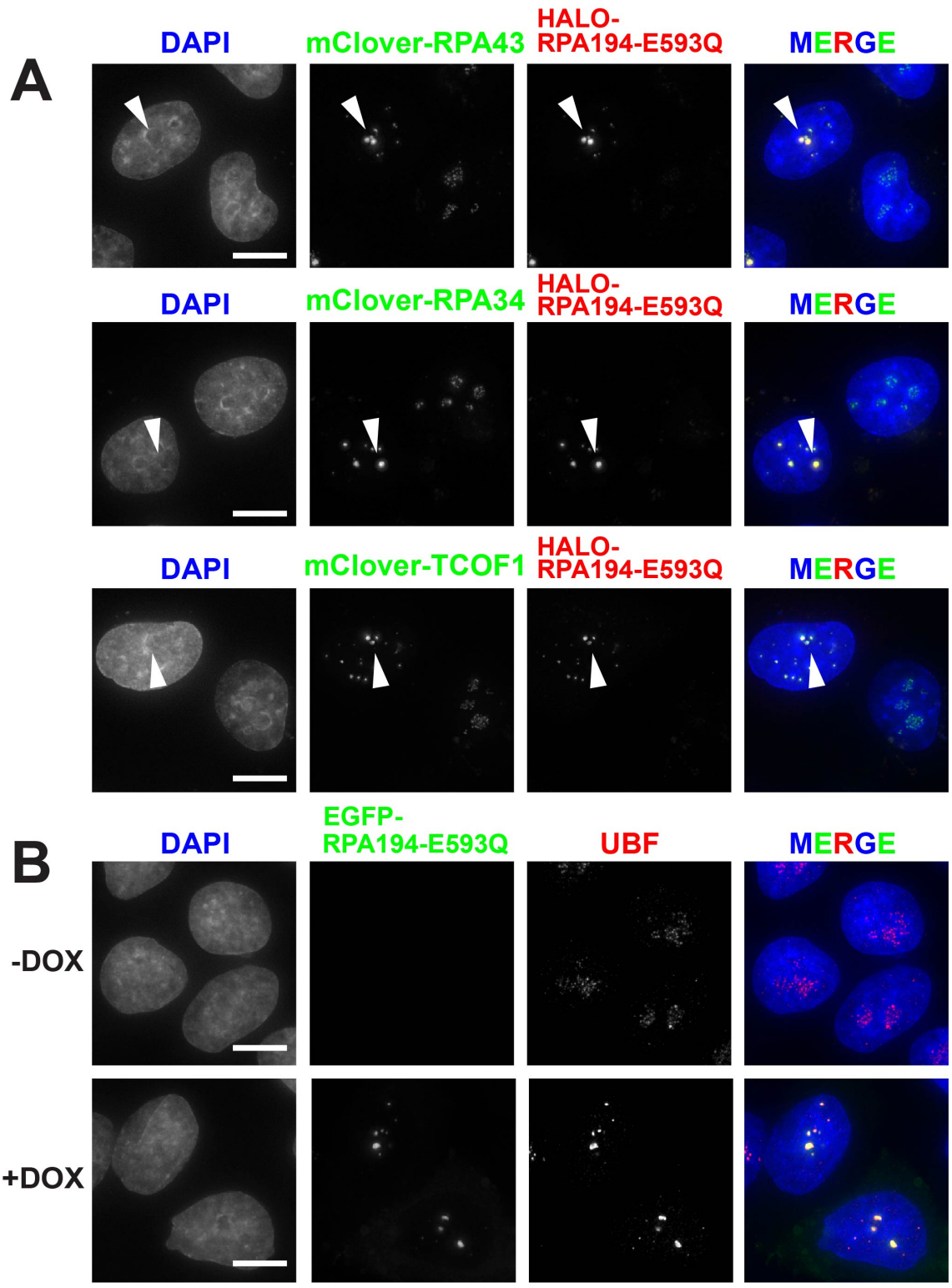
A
DAPI
mClover-RPA43
HALO-RPA194-E593Q
MERGE
DAPI
mClover-RPA34
HALO-RPA194-E593Q
MERGE
DAPI
mClover-TCOF1
HALO-RPA194-E593Q
MERGE
B
DAPI
EGFP-RPA194-E593Q
UBF
MERGE
-DOX
+DOX

fig. S6

**Figure S6. Nucleolar cap components in cells expressing EGFP-RPA194-E593Q.** **(A)** Images of endogenous mClover-RPA43 (first row), mClover-RPA34 (second row), and mClover-TCOF1 (third row) in cells expressing HaloTag-RPA194-E593Q. Note that HaloTag-RPA194-E593Q was fluorescently labeled with an excess amount of the HaloTag ligand TMR. First column, DAPI staining; second column, mClover signals; third column, HaloTag signals; fourth column, merged images. Arrows indicate typical nucleolar caps in cells expressing HaloTag-RPA194-E593Q. Scale bars, 10 μm. **(B)** Localization of UBF in cells following the induction of EGFP-RPA194-E593Q. Cells were grown in the presence or absence of 2 μg/mL doxycycline for 24 h prior to staining with DAPI and anti-UBF antibody. First column, DAPI staining; second column, EGFP-RPA194-E593Q signals; third column, UBF signals; and fourth column, merged images. Scale bars, 10 μm.

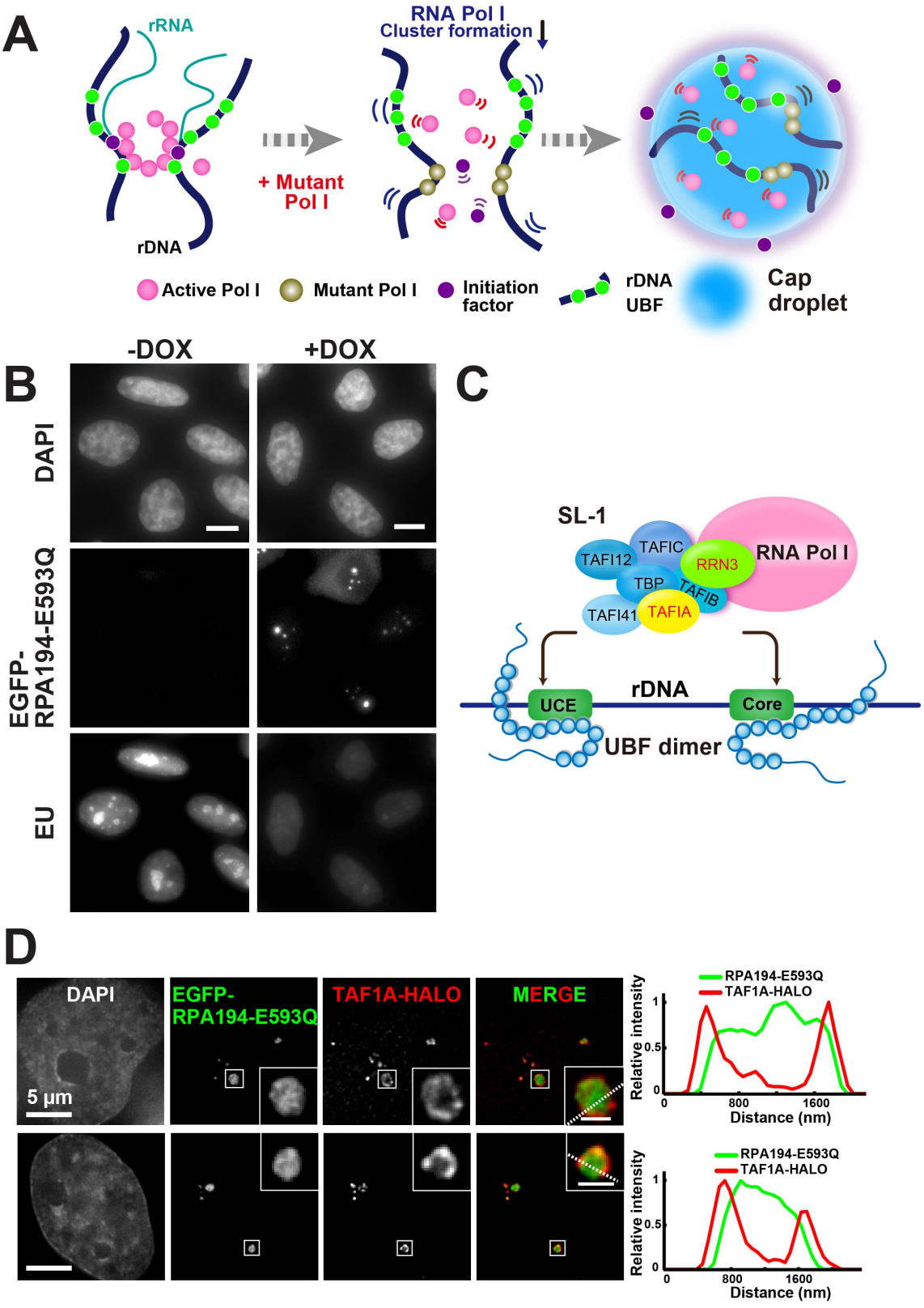
A
rRNA
rDNA
+ Mutant Pol I
RNA Pol I
Cluster formation
Active Pol I
Mutant Pol I
Initiation factor
rDNA
UBF
Cap droplet
B
-DOX
+DOX
DAPI
EGFP-RPA194-E593Q
EU
C
SL-1
TAFI12
TAFIC
RRN3
RNA Pol I
TBP
TAFIB
TAFI41
TAFIA
rDNA
UCE
Core
UBF dimer
D
DAPI
5 µm
EGFP-RPA194-E593Q
TAF1A-HALO
MERGE
RPA194-E593Q
TAF1A-HALO
Relative intensity
Distance (nm)

fig. S7

**Figure S7. Pol I mutant accumulation inhibits rRNA transcription.**
**(A)** Mutant Pol I stably binds to rDNA chromatin and inhibits WT Pol I cluster/condensate formation. The entire Pol I population becomes mobile in the nucleolar cap. **(B)** rRNA synthesis was monitored through addition of 5-ethynyl uridine (EU) before (left column) and after induction of RPA194-E593Q (right column). The EU was conjugated with Alexa Fluor 594. Suppression of transcription was observed upon expression of EGFP-RPA194-E593Q. Scale bars, 10 μm. **(C)** Schematic diagram of the assembly of the Pol I complex at the rDNA promoter. **(Left, D)** Localization of TAF1A-HaloTag (red) in two cells transiently expressing EGFP-RPA194-E593Q. First column, DAPI staining; second column, RPA194 signals (green); third column, TAF1-HaloTag signals (red); fourth column, merged images. Scale bars, 5 μm. Insets show enlarged images of regions indicated with boxes. Scale bars, 1 μm. **(right)** Line plots showing measurements along the white dotted lines in the merged images.

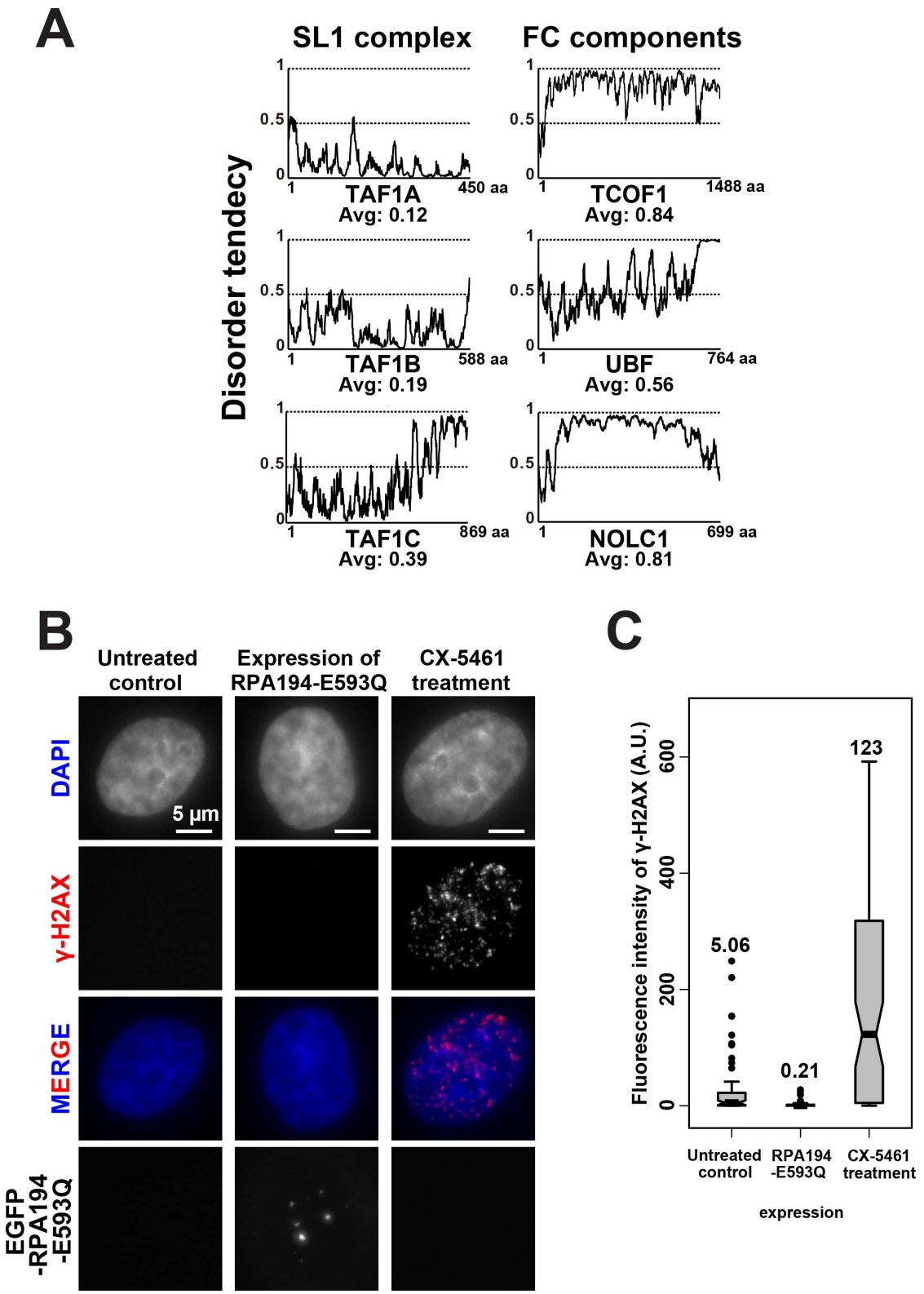
A
SL1 complex
FC components
Disorder tendecy
TAF1A
Avg: 0.12
450 aa
TCOF1
Avg: 0.84
1488 aa
TAF1B
Avg: 0.19
588 aa
UBF
Avg: 0.56
764 aa
TAF1C
Avg: 0.39
869 aa
NOLC1
Avg: 0.81
699 aa
B
Untreated control
Expression of RPA194-E593Q
CX-5461 treatment
DAPI
γ-H2AX
MERGE
EGFP -RPA194 -E593Q
5 μm
C
Fluorescence intensity of γ-H2AX (A.U.)
5.06
0.21
123
Untreated control
RPA194 -E593Q
CX-5461 treatment
expression

fig. S8

**Figure S8.**

**Disorder scores of initiation factors and DNA damage detection in CX-5461-treated cells and EGFP-RPA194-E593Q-expressing cells. (A)** Prediction scores of protein disorder were generated using the IUPred web server (*72*) and plotted against amino-acid residues for each protein. Left, three TATA-box binding protein-associated factors (TAF1A, TAF1B, and TAF1C) that form the SL1 complex. Right, three primary FC components (TCOF1, UBF, and NOLC1). The average (Avg) prediction scores associated with all full-length proteins are indicated. **(B)** γ-H2AX foci in an untreated HeLa control cell (first column), HeLa cell expressing EGFP-RPA194-E593Q for 24 h (second column) and HeLa cell treated with CX-5461 for 2 h (third column). First row, DAPI signals; second row, γ-H2AX signals; third row, merged images; fourth row, EGFP-RPA194-E593Q signals. **(C)** Boxplot of γ-H2AX fluorescence intensity in untreated control cells (control, n = 72), cells expressing RPA194-E593Q (RPA194-E593Q, n = 76), and cells treated with CX-5461(CX-5461, n = 80). The numbers above each box represent median values.

**Supplementary Table S1**

The numbers of trajectories obtained through single-molecule imaging and tracking.

| Figure | Protein | Legend | Number of trajectories |
|---|---|---|---|
| Fig. 1H | HALO-RPA194 | | 6667 |
| Fig. 1I | HALO-RPA194 | | 6667 |
| Fig. 1K | HALO-RPA194 | RPA194 | 10350 |
| Fig. 1K | HALO-UBF | UBF | 14440 |
| Fig. 2C | HALO-RPA194 | Untreated control | 3482 |
| Fig. 2C | HALO-RPA194 | CX-5461 | 516 |
| Fig. 2D | HALO-RPA194 | RP194 | 10350 |
| Fig. 2D | HALO-RPA194 | RPA194 w/ CX-5461 | 3817 |
| Fig. 2D | HALO-UBF | UBF | 5278 |
| Fig. 2D | HALO-UBF | UBF w/ CX-5461 | 3701 |
| Fig. 2E | PAmCherry-RPA194 | Untreated control | 3860 |
| Fig. 2E | PAmCherry-RPA194 | CX-5461 | 4764 |
| Fig. 2G | PAmCherry-RPA194 | Untreated control | 4666 |
| Fig. 2G | PAmCherry-RPA194 | CX-5461 | 2748 |
| Fig. 3C | HALO-RPA194 | WT RPA194 | 9279 |
| Fig. 3C | HALO-RPA194-E593Q | RPA194-E593Q | 7966 |
| Fig. 3C | HALO-RPA194 | WT RPA194 + CX-5461 | 3817 |
| Fig. 4D | HALO-RPA194 | w/o WT RPA194 | 14657 |
| Fig. 4D | HALO-RPA194 | w/ WT RPA194 | 12243 |
| Fig. 4D | HALO-RPA194 | w/o RPA194-E593Q | 14172 |
| Fig. 4D | HALO-RPA194 | w/ RPA194-E593Q | 4217 |
| Fig. 4E | PAmCherry-RPA194-E593Q | RPA194-E593Q | 2360 |
| Fig. 4F | HALO-UBF | w/o RPA194-E593Q | 21788 |
| Fig. 4F | HALO-UBF | w/ RPA194-E593Q | 15048 |
| Fig. 4F | HALO-RPA194-E593Q | RPA194-E593Q | 7966 |
| fig. S3B | HALO-RPA194 | siControl | 19450 |
| fig. S3B | HALO-RPA194 | siFibrillarin | 11903 |
| fig. S3D | HALO-RPA194 | Untreated control | 11741 |
| fig. S3D | HALO-RPA194 | Roscovitine | 10893 |
| fig. S4E | HALO-UBF | CX-5461 | 4122 |
| fig. S4G | HALO-UBF | CX-5461 | 4122 |
| fig. S4G | HALO-UBF | CX-5461 + ΔATP | 3609 |
| fig. S4I | HALO-RPA194 | CX-5461 | 4468 |
| fig. S4I | HALO-RPA194 | CX-5461 + ΔATP | 5378 |

**Supplementary Table S2**.

The primers used in this study.

| Primers | Sequence | Purpose |
|---|---|---|
| dPuromycin-Fw | ATGACCGAGTACAAGCCCACGGTGC | Amplification of puromycin resistant gene |
| dPuromycin-Rv | CGTCTCCTGCTTGCTTTAACAGAGAGAAGTTCGTGGCTCCGGATCCGGCACCGGGCTTGCGGGTCATG | |
| dHygromycin-Fw | ATGAAAAAGCCTGAACTCACCGCGAC | Amplification of hygromycin resistant gene |
| dHygromycin-Rv | CGTCTCCTGCTTGCTTTAACAGAGAGAAGTTCGTGGCTCCGGATCCTTCCTTTGCCCTCGGACGAGTG | |
| N-Halotag-Fw | AGCAAGCAGGAGACGTGGAAGAAAACCCCGGTCCCATGGGATCCGAAATCGGTAC | Amplification of HaloTag sequence |
| N-Halotag-Rv | CGCCGCCACCAGATCCACCTCCACCAGATCCACCTCCACCACCGGAAATCTCCAGAGTAG | |
| dAID-mClover_Fw | TCTCTGTTAAAGCAAGCAGGAGACGTGGAAGAAAACCCCGGTCCCAAGGAGAAGAGTGCTTGTCCTAAAG | Amplification of mAID-mClover sequence |
| dAID-mClover_Rv | CGCCGCCACCAGATCCACCTCCACCAGATCCACCTCCACCCTTGTACAGCTCGTCCATGCCATG | |
| dhUBF-Fw1 | GCGGCCGCGGGAATTCTCCCGCCCTCTCCTTGGCTC | Amplification of homologous arm sequence upstream of the start codon of gene |
| dhUBF-Rv1 | CTTGTACTCGGTCATCCTCCAGCTGTCCAGCCACCTC | |
| dhUBF-Fw2 | TCTGGTGGCGGCGGTTCAATGAACGGAGAAGCCGACTGC | Amplification of homologous arm sequence downstream of the start codon of gene |
| dhUBF-Rv2 | CTCCCATATGGTCGACCTTGTCAGCCCAACTACCCAG | |
| dhUBF_gRNA22-Fw | CACCGTTCCAGGTCTGTGGGGCAGT | Guide RNA for N-terminal tagging of UBF |
| dhUBF_gRNA22-Rv | AAACACTGCCCCACAGACCTGGAAC | |
| dhRPA194-Fw1 | GCGGCCGCGGGAATTCAATAAATGCGTTGCGAATCC | Amplification of homologous arm sequence upstream of the start codon of gene |
| dhRPA194-Rv1 | CTTGTACTCGGTCATCCTCCAGGTCCGTTTTGAATTCC | |
| dhRPA194-Fw2 | TCTGGTGGCGGCGGTTCAATGTTGATCTCCAAGAACATGC | Amplification of homologous arm sequence downstream of the start codon of gene |
| dhRPA194-Rv2 | CTCCCATATGGTCGACCCTTGCTCACCAATGTGTCA | |
| dRPA194_gRNA-Fw | CACCGTGGGGTGTCGGAATTCAAAA | Guide RNA for N-terminal tagging ofRPA194 |
| dRPA194_gRNA-Rv | AAACTTTTGAATTCCGACACCCCAC | |
| dhRPA43-Fw | GCGGCCGCGGGAATTCTTAAACAGGGCACAACACGA | Amplification of homologous arm sequence upstream of the start codon of gene |
| dhRPA43-Rv | TTCAGGCTTTTTCATGCTGCTTGTCAAGGTTCCCACG | |
| dhRPA43-Fw2 | TCTGGTGGCGGCGGTTCAATGGCTGCAGGTTGCTCAGAG | Amplification of homologous arm sequence downstream of the start codon of gene |
| dhRPA43-Rv2 | CTCCCATATGGTCGACCAGAGCGAAATCCAACAACA | |

**Supplementary Table S3**.

The strains used in this study.

| Cell lines | Background | Expression construct | Endogenous or Exogenous | Alleles | Publication |
|---|---|---|---|---|---|
| HeLa S3 FRT-Bla | HeLa S3 | | Exo: Not detemined (FRT) | | Yahata et al. (ref. #73) |
| HeLa S3 HaloTag-RPA194 clone1 | HeLa S3 FRT-Bla | HaloTag-RPA194 | Endo | Monoallele | this paper |
| HeLa S3 HaloTag-RPA194 clone2 | HeLa S3 FRT-Bla | HaloTag-RPA194 | Endo | Biallele | this paper |
| HeLa S3 HaloTag-RPA194 EGFP-Fibrillarin | HeLa S3 HaloTag-RPA194 clone2 | HaloTag-RPA194, pEF1: EGFP-Fibrillarin | Exo: Not detemined (FRT) | | this paper |
| HeLa S3 PAmCherry-RPA194 | HeLa S3 FRT-Bla | PAmCherry-RPA194 | Endo | Monoallele | this paper |
| HeLa S3 HaloTag-UBF | HeLa S3 FRT-Bla | HaloTag-UBF | Endo | Biallele | this paper |
| HeLa S3 HaloTag-RPA194 TetOne-EGFP-RPA194 | HeLa S3 HaloTag-RPA194 clone2 | HaloTag-RPA194, pTet: EGFP-RPA194 | Exo: AAVS1 | Monoallele | this paper |
| HeLa S3 HaloTag-RPA194 TetOne-EGFP-RPA194-E593Q | HeLa S3 HaloTag-RPA194 clone2 | HaloTag-RPA194, pTet: EGFP-RPA194-E593Q | Exo: AAVS1 | Monoallele | this paper |
| HeLa S3 HaloTag-UBF TetOne-EGFP-RPA194-E593Q | HeLa S3 FRT-Bla HaloTag-UBF | HaloTag-UBF, pTet: EGFP-RPA194-E593Q | Exo: AAVS1 | Monoallele | this paper |
| HeLa S3 OsTIR1 | HeLa S3 FRT-Bla | pTet: OsTIR1 | Exo: AAVS1 | | this paper |
| HeLa S3 mClover-RPA43 | HeLa S3 FRT-Bla | mAID-mClover-RPA43 | Endo | Monoallele | this paper |
| HeLa S3 mClover-RPA34 | HeLa S3 FRT-Bla | mAID-mClover-RPA34 | Endo | Monoallele | this paper |
| HeLa S3 mClover-TCOF1 | HeLa S3 FRT-Bla | mAID-mClover-TCOF1 | Endo | Monoallele | this paper |
| HeLa S3 TAF1A-HaloTag | HeLa S3 FRT-Bla | TAF1A-HaloTag | Endo | Monoallele | this paper |
| Hct116 OsTIR1 | HCT116 | pTet: OsTIR1 | Exo: AAVS1 | Biallele | Natsume et al. (ref. #52) |
| Hct116 mAID-mClover-RPA194 | HCT116 OsTIR1 | mAID-mClover-RPA194, pTet: OsTIR1 | Endo | Biallele | this paper |

**Movie S1, related to Figures 1 and 2. Left,** single HaloTag-labeled RPA194 molecules in a live HeLa cell. Nucleoli are indicated by white lines. **Right,** individual HaloTag-labeled RPA194 molecules in a live HeLa cell after treatment with the transcription inhibitor CX-5461. Nucleoli are indicated by white lines.

**REFERENCES AND NOTES**


1. A. A. Hyman, C. A. Weber, F. Jülicher, Liquid-liquid phase separation in biology. *Annu. Rev. Cell Dev. Biol.* **30**, 39–58 (2014).

2. D. T. McSwiggen, M. Mir, X. Darzacq, R. Tjian, Evaluating phase separation in live cells: Diagnosis, caveats, and functional consequences. *Genes Dev.* **33**, 1619–1634 (2019).

3. T. Pederson, The nucleolus. *Cold Spring Harb. Perspect. Biol.* **3**, a000638 (2011).

4. C. P. Brangwynne, T. J. Mitchison, A. A. Hyman, Active liquid-like behavior of nucleoli determines their size and shape in *Xenopus laevis* oocytes. *Proc. Natl. Acad. Sci. U.S.A.* **108**, 4334–4339 (2011).

5. M. Feric, N. Vaidya, T. S. Harmon, D. M. Mitrea, L. Zhu, T. M. Richardson, R. W. Kriwacki, R. V. Pappu, C. P. Brangwynne, Coexisting liquid phases underlie nucleolar subcompartments. *Cell* **165**, 1686–1697 (2016).

6. D. M. Mitrea, J. A. Cika, C. B. Stanley, A. Nourse, P. L. Onuchic, P. R. Banerjee, A. H. Phillips, C.-G. Park, A. A. Deniz, R. W. Kriwacki, Self-interaction of NPM1 modulates multiple mechanisms of liquid–liquid phase separation. *Nat. Commun.* **9**, 842 (2018).

7. D. M. Mitrea, J. A. Cika, C. S. Guy, D. Ban, P. R. Banerjee, C. B. Stanley, A. Nourse, A. A. Deniz, R. W. Kriwacki, Nucleophosmin integrates within the nucleolus via multi-modal interactions with proteins displaying R-rich linear motifs and rRNA. *eLife* **5**, e13571 (2016).

8. H. Mangan, M. Ó. Gailín, B. McStay, Integrating the genomic architecture of human nucleolar organizer regions with the biophysical properties of nucleoli. *FEBS J.* **284**, 3977–3985 (2017).

9. H. Falahati, B. Pelham-Webb, S. Blythe, E. Wieschaus, Nucleation by rRNA dictates the precision of nucleolus assembly. *Curr. Biol.* **26**, 277–285 (2016).

10. H. Falahati, E. Wieschaus, Independent active and thermodynamic processes govern the nucleolus assembly in vivo. *Proc. Natl. Acad. Sci. U.S.A.* **114**, 1335–1340 (2017).

11. R. C. Reynolds, P. O. Montgomery, B. Hughes, Nucleolar "Caps" produced by actinomycin D. *Cancer Res.* **24**, 1269–1277 (1964).

12. E. G. Jordan, J. H. McGovern, The quantitative relationship of the fibrillar centres and other nucleolar components to changes in growth conditions, serum deprivation and low doses of actinomycin D in cultured diploid human fibroblasts (strain MRC-5). *J. Cell Sci.* **52**, 373–389 (1981).

13. P. Tchelidze, A. Benassarou, H. Kaplan, M.-F. O'Donohue, L. Lucas, C. Terryn, L. Rusishvili, G. Mosidze, N. Lalun, D. Ploton, Nucleolar sub-compartments in motion during rRNA synthesis inhibition: Contraction of nucleolar condensed chromatin and gathering of fibrillar centers are concomitant. *PLOS ONE* **12**, e0187977 (2017).

14. J. Russell, J. C. Zomerdijk, RNA-polymerase-I-directed rDNA transcription, life and works. *Trends Biochem. Sci.* **30**, 87–96 (2005).

15. J. S. Andersen, Y. W. Lam, A. K. Leung, S.-E. Ong, C. E. Lyon, A. I. Lamond, M. Mann, Nucleolar proteome dynamics. *Nature* **433**, 77–83 (2005).

16. S. Ide, J. Dejardin, End-targeting proteomics of isolated chromatin segments of a mammalian ribosomal RNA gene promoter. *Nat. Commun.* **6**, 6674 (2015).

17. I. Grummt, Life on a planet of its own: Regulation of RNA polymerase I transcription in the nucleolus. *Genes Dev.* **17**, 1691–1702 (2003).

18. T. Moss, At the crossroads of growth control; making ribosomal RNA. *Curr. Opin. Genet. Dev.* **14**, 210–217 (2004).

19. S. Ide, T. Miyazaki, H. Maki, T. Kobayashi, Abundance of ribosomal RNA gene copies maintains genome integrity. *Science* **327**, 693–696 (2010).

20. Y. Takeuchi, T. Horiuchi, T. Kobayashi, Transcription-dependent recombination and the role of fork collision in yeast rDNA. *Genes Dev.* **17**, 1497–1506 (2003).

21. D. Chen, S. Huang, Nucleolar components involved in ribosome biogenesis cycle between the nucleolus and nucleoplasm in interphase cells. *J. Cell Biol.* **153**, 169–176 (2001).

22. M. Dundr, U. Hoffmann-Rohrer, Q. Hu, I. Grummt, L. I. Rothblum, R. D. Phair, T. Misteli, A kinetic framework for a mammalian RNA polymerase in vivo. *Science* **298**, 1623–1626 (2002).

23. S. A. Gorski, S. K. Snyder, S. John, I. Grummt, T. Misteli, Modulation of RNA polymerase assembly dynamics in transcriptional regulation. *Mol. Cell* **30**, 486–497 (2008).

24. J. O. Andrews, W. Conway, W.-K. Cho, A. Narayanan, J.-H. Spille, N. Jayanth, T. Inoue, S. Mullen, J. Thaler, I. I. Cissé, qSR: A quantitative super-resolution analysis tool reveals the cell-cycle dependent organization of RNA Polymerase I in live human cells. *Sci. Rep.* **8**, 7424 (2018).

25. I. I. Cisse, I. Izeddin, S. Z. Causse, L. Boudarene, A. Senecal, L. Muresan, C. Dugast-Darzacq, B. Hajj, M. Dahan, X. Darzacq, Real-time dynamics of RNA polymerase II clustering in live human cells. *Science* **341**, 664–667 (2013).

26. W.-K. Cho, J.-H. Spille, M. Hecht, C. Lee, C. Li, V. Grube, I. I. Cissé, Mediator and RNA polymerase II clusters associate in transcription-dependent condensates. *Science* **361**, 412–415 (2018).

27. T. Nozaki, R. Imai, M. Tanbo, R. Nagashima, S. Tamura, T. Tani, Y. Joti, M. Tomita, K. Hibino, M. T. Kanemaki, K. S. Wendt, Y. Okada, T. Nagai, K. Maeshima, Dynamic organization of chromatin domains revealed by super-resolution live-cell imaging. *Mol. Cell* **67**, 282–293.e7 (2017).

28. R. Nagashima, K. Hibino, S. S. Ashwin, M. Babokhov, S. Fujishiro, R. Imai, T. Nozaki, S. Tamura, T. Tani, H. Kimura, M. Shribak, M. T. Kanemaki, M. Sasai, K. Maeshima, Single nucleosome imaging reveals loose genome chromatin networks via active RNA polymerase II. *J. Cell Biol.* **218**, 1511–1530 (2019).

29. S. S. Ashwin, T. Nozaki, K. Maeshima, M. Sasai, Organization of fast and slow chromatin revealed by single-nucleosome dynamics. *Proc. Natl. Acad. Sci. U.S.A.* **116**, 19939–19944 (2019).

30. K. N. Weaver, K. E. N. Watt, R. B. Hufnagel, J. Navajas Acedo, L. L. Linscott, K. L. Sund, P. L. Bender, R. König, C. M. Lourenco, U. Hehr, R. J. Hopkin, D. R. Lohmann, P. A. Trainor, D. Wieczorek, H. M. Saal, Acrofacial dysostosis, cincinnati type, a mandibulofacial dysostosis syndrome with limb anomalies, is caused by *POLR1A* dysfunction. *Am. J. Hum. Genet.* **96**, 765–774 (2015).

31. P. Seither, J. F. Coy, A. Pouska, I. Grummt, Molecular cloning and characterization of the cDNA encoding the largest subunit of mouse RNA polymerase I. *Mol. Gen. Genet.* **255**, 180–186 (1997).

32. S. Hihara, C.-G. Pack, K. Kaizu, T. Tani, T. Hanafusa, T. Nozaki, S. Takemoto, T. Yoshimi, H. Yokota, N. Imamoto, Y. Sako, M. Kinjo, K. Takahashi, T. Nagai, K. Maeshima, Local nucleosome dynamics facilitate chromatin accessibility in living mammalian cells. *Cell Rep.* **2**, 1645–1656 (2012).

33. M. Tokunaga, N. Imamoto, K. Sakata-Sogawa, Highly inclined thin illumination enables clear single-molecule imaging in cells. *Nat. Methods* **5**, 159–161 (2008).

34. V. Dion, S. M. Gasser, Chromatin movement in the maintenance of genome stability. *Cell* **152**, 1355–1364 (2013).

35. P. Hozák, P. R. Cook, C. Schöfer, W. Mosgöller, F. Wachtler, Site of transcription of ribosomal RNA and intranucleolar structure in HeLa cells. *J. Cell Sci.* **107**, 639–648 (1994).

36. T. Cheutin, M.-F. O'Donohue, A. Beorchia, M. Vandelaer, H. Kaplan, B. Deféver, D. Ploton, M. Thiry, Three-dimensional organization of active rRNA genes within the nucleolus. *J. Cell Sci.* **115**, 3297–3307 (2002).

37. D. Tollervey, H. Lehtonen, R. Jansen, H. Kern, E. C. Hurt, Temperature-sensitive mutations demonstrate roles for yeast fibrillarin in pre-rRNA processing, pre-rRNA methylation, and ribosome assembly. *Cell* **72**, 443–457 (1993).

38. V. Sirri, D. Hernandez-Verdun, P. Roussel, Cyclin-dependent kinases govern formation and maintenance of the nucleolus. *J. Cell Biol.* **156**, 969–981 (2002).

39. D. P. Bazett-Jones, B. Leblanc, M. Herfort, T. Moss, Short-range DNA looping by the Xenopus HMG-box transcription factor, xUBF. *Science* **264**, 1134–1137 (1994).

40. A. C. O'Sullivan, G. J. Sullivan, B. McStay, UBF binding in vivo is not restricted to regulatory sequences within the vertebrate ribosomal DNA repeat. *Mol. Cell. Biol.* **22**, 657–668 (2002).

41. M. Babokhov, K. Hibino, Y. Itoh, K. Maeshima, Local chromatin motion and transcription. *J. Mol. Biol.* **432**, 694–700 (2020).

42. P. R. Cook, The organization of replication and transcription. *Science* **284**, 1790–1795 (1999).

43. L. B. Edelman, P. Fraser, Transcription Factories: Genetic Programming in Three Dimensions. *Curr. Opin. Genet. Dev.* **22**, 110–114 (2012).

44. D. Drygin, A. Lin, J. Bliesath, C. B. Ho, S. E. O'Brien, C. Proffitt, M. Omori, M. Haddach, M. K. Schwaebe, A. Siddiqui-Jain, N. Streiner, J. E. Quin, E. Sanij, M. J. Bywater, R. D. Hannan, D. Ryckman, K. Anderes, W. G. Rice, Targeting RNA polymerase I with an oral small molecule CX-5461 inhibits ribosomal RNA synthesis and solid tumor growth. *Cancer Res.* **71**, 1418–1430 (2011).

45. J. Quin, K. T. Chan, J. R. Devlin, D. P. Cameron, J. Diesch, C. Cullinane, J. Ahern, A. Khot, N. Hein, A. J. George, K. M. Hannan, G. Poortinga, K. E. Sheppard, K. K. Khanna, R. W. Johnstone, D. Drygin, G. A. McArthur, R. B. Pearson, E. Sanij, R. D. Hannan, Inhibition of RNA polymerase I transcription initiation by CX-5461 activates non-canonical ATM/ATR signaling. *Oncotarget* **7**, 49800–49818 (2016).

46. H. Hajjoul, J. Mathon, H. Ranchon, I. Goiffon, J. Mozziconacci, B. Albert, P. Carrivain, J.-M. Victor, O. Gadal, K. Bystricky, A. Bancaud, High-throughput chromatin motion tracking in living yeast reveals the flexibility of the fiber throughout the genome. *Genome Res.* **23**, 1829–1838 (2013).

47. F. V. Subach, G. H. Patterson, S. Manley, J. M. Gillette, J. Lippincott-Schwartz, V. V. Verkhusha, Photoactivatable mCherry for high-resolution two-color fluorescence microscopy. *Nat. Methods* **6**, 153–159 (2009).

48. Y. Sakamoto, M. Ishiguro, G. Kitagawa, *Akaike Information Criterion Statistics* (KTK Scientific Publishers; D. Reidel; Sold and distributed in the U.S.A. and Canada by Kluwer Academic Publishers, Tokyo Dordrecht; Boston Hingham, MA, 1986).

49. C. Y. Jao, A. Salic, Exploring RNA transcription and turnover in vivo by using click chemistry. *Proc. Natl. Acad. Sci. U.S.A.* **105**, 15779–15784 (2008).

50. D. K. Trask, M. T. Muller, Stabilization of type I topoisomerase-DNA covalent complexes by actinomycin D. *Proc. Natl. Acad. Sci. U.S.A.* **85**, 1417–1421 (1988).

51. H. Xu, M. Di Antonio, S. McKinney, V. Mathew, B. Ho, N. J. O'Neil, N. D. Santos, J. Silvester, V. Wei, J. Garcia, F. Kabeer, D. Lai, P. Soriano, J. Banáth, D. S. Chiu, D. Yap, D. D. Le, F. B. Ye, A. Zhang, K. Thu, J. Soong, S.-C. Lin, A. H. C. Tsai, T. Osako, T. Algara, D. N. Saunders, J. Wong, J. Xian, M. B. Bally, J. D. Brenton, G. W. Brown, S. P. Shah, D. Cescon, T. W. Mak, C. Caldas, P. C. Stirling, P. Hieter, S. Balasubramanian, S. Aparicio, CX-5461 is a DNA G-quadruplex stabilizer with selective lethality in BRCA1/2 deficient tumours. *Nat. Commun.* **8**, 14432 (2017).

52. T. Natsume, T. Kiyomitsu, Y. Saga, M. T. Kanemaki, Rapid protein depletion in human cells by auxin-inducible degron tagging with short homology donors. *Cell Rep.* **15**, 210–218 (2016).

53. R.-W. Yao, G. Xu, Y. Wang, L. Shan, P.-F. Luan, Y. Wang, M. Wu, L.-Z. Yang, Y.-H. Xing, L. Yang, L.-L. Chen, Nascent pre-rRNA sorting via phase separation drives the assembly of dense fibrillar components in the human nucleolus. *Mol. Cell* **76**, 767–783.e11 (2019).

54. L. Zhu, T. M. Richardson, L. Wacheul, M.-T. Wei, M. Feric, G. Whitney, D. L. J. Lafontaine, C. P. Brangwynne, Controlling the material properties and rRNA processing function of the nucleolus using light. *Proc. Natl. Acad. Sci. U.S.A.* **116**, 17330–17335 (2019).

55. F. Frottin, F. Schueder, S. Tiwary, R. Gupta, R. Körner, T. Schlichthaerle, J. Cox, R. Jungmann, F. U. Hartl, M. S. Hipp, The nucleolus functions as a phase-separated protein quality control compartment. *Science* **365**, 342–347 (2019).

56. N. O. Taylor, M.-T. Wei, H. A. Stone, C. P. Brangwynne, Quantifying dynamics in phase-separated condensates using fluorescence recovery after photobleaching. *Biophys. J.* **117**, 1285–1300 (2019).

57. M. Kruhlak, E. E. Crouch, M. Orlov, C. Montaño, S. A. Gorski, A. Nussenzweig, T. Misteli, R. D. Phair, R. Casellas, The ATM repair pathway inhibits RNA polymerase I transcription in response to chromosome breaks. *Nature* **447**, 730–734 (2007).

58. M. van Sluis, B. McStay, A localized nucleolar DNA damage response facilitates recruitment of the homology-directed repair machinery independent of cell cycle stage. *Genes Dev.* **29**, 1151–1163 (2015).

59. W. K. Cho, N. Jayanth, B. P. English, T. Inoue, J. O. Andrews, W. Conway, J. B. Grimm, J. H. Spille, L. D. Lavis, T. Lionnet, I. I. Cissé, RNA Polymerase II cluster dynamics predict mRNA output in living cells. *eLife* **5**, e13617 (2016).

60. M. Boehning, C. Dugast-Darzacq, M. Rankovic, A. S. Hansen, T. Yu, H. Marie-Nelly, D. T. McSwiggen, G. Kokic, G. M. Dailey, P. Cramer, X. Darzacq, M. Zweckstetter, RNA polymerase II clustering through carboxy-terminal domain phase separation. *Nat. Struct. Mol. Biol.* **25**, 833–840 (2018).

61. A. Boija, I. A. Klein, B. R. Sabari, A. Dall'Agnese, E. L. Coffey, A. V. Zamudio, C. H. Li, K. Shrinivas, J. C. Manteiga, N. M. Hannett, B. J. Abraham, L. K. Afeyan, Y. E. Guo, J. K. Rimel, C. B. Fant, J. Schuijers, T. I. Lee, D. J. Taatjes, R. A. Young, Transcription factors activate genes through the phase-separation capacity of their activation domains. *Cell* **175**, 1842–1855.e16 (2018).

62. S. Chong, C. Dugast-Darzacq, Z. Liu, P. Dong, G. M. Dailey, C. Cattoglio, A. Heckert, S. Banala, L. Lavis, X. Darzacq, R. Tjian, Imaging dynamic and selective low-complexity domain interactions that control gene transcription. *Science* **361**, eaar2555 (2018).

63. B. R. Sabari, A. Dall'Agnese, A. Boija, I. A. Klein, E. L. Coffey, K. Shrinivas, B. J. Abraham, N. M. Hannett, A. V. Zamudio, J. C. Manteiga, C. H. Li, Y. E. Guo, D. S. Day, J. Schuijers, E. Vasile, S. Malik, D. Hnisz, T. I. Lee, I. I. Cisse, R. G. Roeder, P. A. Sharp, A. K. Chakraborty, R. A. Young, Coactivator condensation at super-enhancers links phase separation and gene control. *Science* **361**, eaar3958 (2018).

64. A. P. Ross, K. S. Zarbalis, The emerging roles of ribosome biogenesis in craniofacial development. *Front. Physiol.* **5**, 26 (2014).

65. J. G. Dauwerse, J. Dixon, S. Seland, C. A. Ruivenkamp, A. van Haeringen, L. H. Hoefsloot, D. J. Peters, A. C. Boers, C. Daumer-Haas, R. Maiwald, C. Zweier, B. Kerr, A. M. Cobo, J. F. Toral, A. J. Hoogeboom, D. R. Lohmann, U. Hehr, M. J. Dixon, M. H. Breuning, D. Wieczorek, Mutations in genes encoding subunits of RNA polymerases I and III cause Treacher Collins syndrome. *Nat. Genet.* **43**, 20–22 (2011).

66. K. Maeshima, K. Yahata, Y. Sasaki, R. Nakatomi, T. Tachibana, T. Hashikawa, F. Imamoto, N. Imamoto, Cell-cycle-dependent dynamics of nuclear pores: Pore-free islands and lamins. *J. Cell Sci.* **119**, 4442–4451 (2006).

67. F. A. Ran, P. D. Hsu, J. Wright, V. Agarwala, D. A. Scott, F. Zhang, Genome engineering using the CRISPR-Cas9 system. *Nat. Protoc.* **8**, 2281–2308 (2013).

68. M. A. Mandegar, N. Huebsch, E. B. Frolov, E. Shin, A. Truong, M. P. Olvera, A. H. Chan, Y. Miyaoka, K. Holmes, C. I. Spencer, L. M. Judge, D. E. Gordon, T. V. Eskildsen, J. E. Villalta, M. A. Horlbeck, L. A. Gilbert, N. J. Krogan, S. P. Sheikh, J. S. Weissman, L. S. Qi, P.-L. So, B. R. Conklin, CRISPR interference efficiently induces specific and reversible gene silencing in human iPSCs. *Cell Stem Cell* **18**, 541–553 (2016).

69. A. Park, S. T. Won, M. Pentecost, W. Bartkowski, B. Lee, CRISPR/Cas9 allows efficient and complete knock-in of a destabilization domain-tagged essential protein in a human cell line, allowing rapid knockdown of protein function. *PLOS ONE* **9**, e95101 (2014).

70. J. Schindelin, I. Arganda-Carreras, E. Frise, V. Kaynig, M. Longair, T. Pietzsch, S. Preibisch, C. Rueden, S. Saalfeld, B. Schmid, J.-Y. Tinevez, D. J. White, V. Hartenstein, K. Eliceiri, P. Tomancak, A. Cardona, Fiji: An open-source platform for biological-image analysis. *Nat. Methods* **9**, 676–682 (2012).

71. K. Jaqaman, D. Loerke, M. Mettlen, H. Kuwata, S. Grinstein, S. L. Schmid, G. Danuser, Robust single-particle tracking in live-cell time-lapse sequences. *Nat. Methods* **5**, 695–702 (2008).

72. Z. Dosztányi, V. Csizmok, P. Tompa, I. Simon, IUPred: Web server for the prediction of intrinsically unstructured regions of proteins based on estimated energy content. *Bioinformatics* **21**, 3433–3434 (2005).

73. K. Yahata, K. Maeshima, T. Sone, T. Ando, M. Okabe, N. Imamoto, F. Imamoto, cHS4 insulator-mediated alleviation of promoter interference during cell-based expression of tandemly associated transgenes. *J. Mol. Biol.* **374**, 580–90 (2007).